Title: Structural basis for FLCN RagC GAP activation in MiT-TFE substrate-selective mTORC1 regulation

Authors: Rachel M. Jansen[1,2], Roberta Peruzzo[1], Simon A. Fromm[1,2,†], Adam L. Yokom[1,2] Roberto Zoncu[1,2] and James H. Hurley[1,2,3*]

Affiliations:

[1]Department of Molecular and Cell Biology, University of California Berkeley; Berkeley CA 94720, USA.

[2]California Institute for Quantitative Biosciences, University of California, Berkeley, CA, 94720, USA

[3]Helen Wills Neuroscience Institute, University of California, Berkeley, Berkeley, CA 94720, USA

†Present address: Imaging Centre, European Molecular Biology Laboratory, Heidelberg, Germany

*Corresponding author: jimhurley@berkeley.edu

Abstract

mTORC1 regulates cell growth and catabolism in response to fluctuations in nutrients through phosphorylation of key substrates. The tumor suppressor FLCN is a RagC/D GTPase activating protein (GAP) that regulates mTORC1 phosphorylation of MiT-TFE family transcription factors, controlling lysosome biogenesis and autophagy. Here, we determined the cryo-EM structure of the active FLCN complex (AFC) containing FLCN, FNIP2, the N-terminal tail of SLC38A9, the $RagA^{GDP}$:$RagC^{GDP.BeFx-}$ GTPase dimer, and the Ragulator scaffold. Relative to the inactive lysosomal FLCN complex (LFC) structure, FLCN reorients by 90º, breaks its contacts with RagA, and makes new contacts with RagC that position its Arg164 finger for catalysis. Disruption of the AFC-specific interfaces of FLCN and FNIP2 with RagC eliminated GAP activity in vitro and led to nuclear retention of the MiT-TFE family member TFE3, with no effect on mTORC1 phosphorylation of S6K or 4E-BP1. The structure thus provides a structural basis for the regulation of an mTORC1 substrate-specific pathway and a roadmap to discover MiT-TFE family selective mTORC1 antagonists.

The mechanistic target of rapamycin complex 1 (mTORC1) plays a central role in the response to fluctuations in nutrients, growth factors, and energy in cells by altering the balance between cell growth and catabolism. In nutrient-rich environments, mTORC1 activates anabolic processes including protein and lipid synthesis while inhibiting catabolic ones such as autophagy (*1, 2*). mTORC1 regulates its pro-anabolic programs through phosphorylation of key targets, some of which contain a conserved TOS motif (*3, 4*). The microphthalmia (MiT-TFE) family of transcription factors, including similarly regulated transcription factors EB and E3 (TFEB and TFE3), are pro-catabolic mTORC1 substrates that activate autophagy and lysosome biogenesis (*5, 6*). Among well-known mTORC1 substrates, MiT-TFE family members lack the TOS motif responsible for docking some other substrates onto mTORC1 via its Raptor subunit. Also, in contrast to other mTORC1 substrates, MiT-TFE phosphorylation and negative regulation are completely dependent on the activity of the RagC GAP, FLCN (*7-9*).

The Rag-Ragulator complex consists of two Rag guanosine triphosphatases (commonly referred to as Rags) that function as obligate heterodimers and are anchored to the lysosomal membrane by the pentameric Ragulator (*10, 11*). The Rags respond to lysosomal and cytoplasmic nutrient levels, which regulate the proportion of inactive (RagA or B^{GDP}:RagC or D^{GTP}) and active (RagA or B^{GTP}:RagC or D^{GDP}) Rag dimers (*12*). Conversion between active and inactive states is regulated by the RagA/B-specific GAP, GATOR1, and by the RagC/D-specific GAP, folliculin: folliculin interacting protein 2 (FLCN:FNIP2) (*13, 14*). In response to amino acid levels, as sensed by the transceptor SLC38A9 among other mechanisms (*15-17*), FLCN stimulates the conversion of Rags to their active form enabling mTORC1 recruitment and interaction with MiT-TFE members. Upon phosphorylation, MiT-TFE members bind to 14-3-3 proteins and is sequestered in the cytosol where they remain inactive. The regulation of TOS motif-containing mTORC1 substrates (*3*), including regulators of mRNA translation and cell proliferation, such as 4E-BP1 and S6K1 is unaffected (*7, 8, 18*). Taken together, FLCN directly and selectively controls mTORC1 regulation of MiT-TFE members but not other substrates (*7, 8*). These findings support the existence of separate mechanisms for control of mTORC1-dependent anabolic versus catabolic programs (*19*), and highlight a therapeutic potential for FLCN to be targeted as a means of mTOR inhibition for treating LSDs and neurodegenerative diseases, with fewer toxic effects on cell proliferation and translation.

The transient nature of the GAP interaction with Rag-Ragulator has proven challenging for visualizing details necessary for deducing the mechanism of GAP activity. Previous structural investigation into FLCN interaction with Rag-Ragulator revealed a stable inhibited complex, the lysosomal folliculin complex (LFC) (*8, 20*). This begged the question as to how FLCN binds to RagC to promote nucleotide hydrolysis, and what are the interfaces in FLCN essential for stimulating catalysis? We sought to understand how these residues interact with the RagC nucleotide binding pocket, and what makes FLCN specific for RagC. We previously found that the amino acid transporter, SLC38A9, promotes FLCN GAP activity by inserting its cytosolic domain in the cleft between the RagA and C G-domains and thereby disrupting the

LFC (*16*). Here, we trapped FLCN in its GAP-competent binding mode using a fusion construct with the N-terminal of SLC38A9 ($SLC38A9^{NT}$), determined the cryo-EM structure, and deduced the mechanism of FLCN GAP activity essential for interrogating this interaction during drug development.

Results

To provide a structural framework for understanding the mechanism of FLCN GAP activity, we stabilized the transient complex and determined the cryo-EM structure, hereafter referred to as the Active Folliculin Complex (AFC). We began by generating a stable complex of FLCN:FNIP2, Rags, Ragulator and $SLC38A9^{NT}$, utilizing a mutant $FLCN^{F118D}$ known to disrupt the LFC without affecting GAP activity (*8*). To tether FLCN to the Rag-Ragulator complex, we designed a fusion construct containing a 10-residue glycine-serine linker between the C-terminus of $SLC38A9^{NT}$ and the N-terminus of FNIP2 (Fig. 1A). The C-terminal tail of $SLC38A9^{NT}$ contains ~20 disordered residues, effectively increasing the linker length to ~30 residues allowing for up to 90 Å in length. We used a phosphate analog (BeF_3) during complex formation to capture $FLCN^{F118D}$ bound to Rag-Ragulator (*21*). Rags were loaded into a state mimicking starvation conditions ($RagA^{GDP}$:$RagC^{GTP}$) and incubated with Ragulator to form a stable complex. Next, $FLCN^{F118D}$ and the $SLC38A9^{NT}$-FNIP2 (SLC-FNIP2) fusion protein were added to $RagA^{GDP}$:$RagC^{GTP}$ – Ragulator immediately followed by addition of BeF_3 (Fig. S1). Incubating the complex overnight, we generated a nucleotide ground-state analog that trapped $FLCN^{F118D}$ in an active conformation and allowed for isolation of a stable active FLCN complex via size exclusion chromatography (Fig. 1B, 1C).

The cryo-EM structure of the AFC was determined to an overall resolution of 3.5 Å (Table 1, Fig. S2). The cryo-EM density was of sufficient quality to model the ordered mass of the complex constituting the AFC (Fig. S3 and S4). In the AFC, the longin domains of $FLCN^{F118D}$ and FNIP2 interact with the RagC G-domain such that the $FLCN^{F118D}$:FNIP2 approaches Rag-Ragulator from the side (Fig. 2B, 2C). The $SLC38A9^{NT}$ sits in the cleft between the Rags and does not interact directly with $FLCN^{F118D}$:FNIP2, suggesting it does not play a role in positioning the GAP. The overall dimensions of the complex are ~120 Å by ~180 Å (Fig. 2C). To interact with RagC in a GAP-competent conformation, $FLCN^{F118D}$:FNIP2 reorients 90 degrees and transitions from its elongated position in the LFC to bind the side of RagC in the AFC (Movie S1). In the LFC, FLCN:FNIP2 interacts with both RagC and RagA extensively, with 870 $Å^2$ and 645 $Å^2$ interfaces, respectively. In contrast, in the AFC conformation, $FLCN^{F118D}$:FNIP2 interacts solely with RagC, burying 1,141 $Å^2$ of surface area with RagC, but none with RagA.

To visualize the AFC catalytic complex in as much detail as possible, we used local refinement at the FLCN-RagC interface to increase the resolution to 3.16 Å and allow for clear placement of the nucleotide analog and previously identified arginine finger (Arg-164) in RagC nucleotide-binding domain (NBD) (*8*) (Fig. S2 and S3D). As bound to GDP-BeF^-_3, RagC adopts an architecture analogous to GTP-bound RagC and Gtr2 (*22, 23*) (Fig. 3A). In this state, the

switch I region is ordered and forms a lid at the top of the binding pocket. Additional density in the RagC NBD, adjacent to the BeF^-_3, aligned with the placement of the highly conserved Arg-164. The position of $FLCN^{F118D}$ Arg-164 resembled the geometry of previously identified arginine fingers in Rab1 GAP structures trapped with BeF^-_3 nucleotide analogs (*24, 25*) (Fig. S5). The nucleotide binding pocket is composed of primarily charged residues with a 534 $Å^2$ surface area, while the overall volume of the larger surrounding pocket is 865 $Å^3$ (*26*) (Fig. 3B).

To determine the basis for FLCN specificity for RagC over RagA, we modeled the GAP interaction with RagA-GTP. The $FLCN^{F118D}$ loop containing residues 10-16 was accommodated when interacting with RagC (Fig. 3C). In contrast, in the RagA model, $FLCN^{F118D}$ (Phe^{16}, His^{14}, Pro^{16}) clashed with RagA at the interface (Fig. 3D). We sought to further explore FLCN specificity for RagC by understanding why GATOR1 does not function as a GAP for RagC. We modelled RagC with GATOR1 and observed residues in GATOR1 (Thr^{18} and Pro^{19}) that clashed with RagC at the interface (Fig. S6B). We also compared the RagC structure to that of Arf1, which is a substrate of another longin domain GAP, SMCR8 (*27, 28*). In the Arf1 model, $FLCN^{F118D}$ (Leu^{13} and His^{14}) clash with Arf1 residues (Fig. S6A), rationalizing specificity for RagC. To determine why other longin domain GAPs do not function to stimulate nucleotide hydrolysis of RagC, we modelled RagC with SMCR8, a longin GAP that acts on Arf GTPases. The binding between SMCR8 and RagC is incompatible due to clashes between SMCR8 (Glu^{62} and Phe^{63}) and RagC (Fig. S6C).

We analyzed the interface whereby $FLCN^{F118D}$:FNIP2 interacts with RagC. Two hydrophobic residues FLCN Phe10 and FNIP2 Val146 form prominent contacts in the RagC binding interface interacting with Thr96, Lys78, Met121 and Phe128 (Fig. 4A). We hypothesized that these residues were critical for GAP activity. To validate the importance of these residues, we created two mutants $FLCN^{F118D/F10D}$ (F10D:Phe^{10}→Asp) and $FNIP2^{V146E}$ (V146E:Val^{146}→Glu). We used a tryptophan-based GAP activity assay to monitor the activity of $FLCN^{F118D}$:FNIP2 and mutants $FLCN^{F118D/F10D}$:FNIP2 and $FLCN^{F118D}$:$FNIP2^{V146E}$ toward inactive Rags ($RagA^{GDP}$:$RagC^{GTP}$) (*8, 16*). The GAP activity of the $FLCN^{F118D}$:SLC-FNIP2 fusion protein was identical to the $FLCN^{F118D}$:FNIP2 without the SLC38A9 N-terminus fusion (Fig. S7). Both $FLCN^{F118D/F10D}$:FNIP2 and $FLCN^{F118D}$:$FNIP2^{V146E}$ abolished GAP activity as compared to $FLCN^{F118D}$:FNIP2 confirming their importance in facilitating GAP binding (Fig. 4).

We sought to investigate whether these GAP-inactive mutants, $FLCN^{F10D}$ and $FNIP2^{V146E}$, affected the ability of Rag-Ragulator to activate mTORC1 with respect to its various substrates. We used cell-based assays to image the localization of MiT-TFE family transcription factor TFE3. In amino-acid deprived cells reconstituted with either WT FLCN ($FLCN^{WT}$) or WT FNIP2 ($FNIP2^{WT}$), both $FLCN^{WT}$ and $FNIP2^{WT}$ were localized to the lysosome (Fig. 4G) and TFE3 was present in the nucleus (Fig. 4C and 4G). Cells expressing $FLCN^{F10D}$ and $FNIP2^{V146E}$ during starvation resulted in lysosomal localization and nuclear localization of the MiT-TFE family member TFE3 (Fig. 4C, 4E, and 4G). When cells were restimulated with amino acids, those reconstituted with $FLCN^{WT}$ and $FNIP2^{WT}$ resulted in translocation of TFE3 to the cytoplasm. In contrast, in cells expressing $FLCN^{F10D}$ and $FNIP2^{V146E}$ TFE3 remained nuclear,

phenocopying the catalytic loss-of-function mutant FLCN^{R164} (*8*) (Fig. S8) and was not sequestered to the cytoplasm despite high cellular nutrients (Fig. 4C, 4E). These results further supported that the mutants FLCN^{F10D} and FNIP2^{V146E} eliminated GAP activity and confirmed that loss of GAP activity resulted in mis-regulation of mTORC1 and TFE3. Immunoblot analysis confirmed that the mutants did not have any effect on the phosphorylation of the TOS-motif containing substrates S6K and 4E-BP1 (Fig. S9).

Discussion

The cryo-EM structure presented in this work reveals that FLCN:FNIP2 undergoes a dramatic re-orientation to convert from the inactive LFC to the active AFC. The AFC structure confirmed the prediction that FLCN activates nucleotide hydrolysis of RagC through the catalytic arginine finger Arg-164 (*8, 29*). We identified features on the FLCN surface that are complementary to RagC and confer the high degree of specificity that is seen biologically. Our structure revealed that the loop containing residues 10-16 in FLCN make it incompatible as a GAP for other small GTPases. In the AFC structure, SLC38A9^{NT} sits in the cleft between the Rags, while FLCN:FNIP2 binds only RagC. This confirms the previously proposed model that SLC38A9^{NT} displaces inactive FLCN:FNIP2 in the LFC to allow for binding in the GAP competent mode (*16*). SLC38A9^{NT} does not, however, play a role in GAP activity through interaction with FLCN or either Rag nucleotide binding pocket in the AFC, as further supported by the near-identical RagC-GAP activity of FLCN^{F118D}:FNIP2 with or without the SLC38A9^{NT} fusion.

RagA is regulated by a different GAP complex, GATOR1. A recent cryo-EM structure of the GAP-competent interaction between Rag-Ragulator and GATOR1 suggested GATOR1 is stabilized by both Rag GTPases in its GAP mode (*30*). The overall geometry and the role of the Arg finger in the active GATOR1 complex resembles that of FLCN^{F118D}:FNIP2 seen here, as well as that of another longin-domain based GAP, the C9orf72-SMCR8 complex with ARF1 (*27*). In comparison to GATOR1, the structure of the AFC revealed that FLCN solely interacts with RagC to stimulate GTP hydrolysis. This finding is consistent with observations that while GATOR1 RagA GAP activity depends on the RagC nucleotide state, the RagC GAP activity of the AFC is independent of the RagA nucleotide state (*16*).

The past few years have seen a paradigm shift in understanding how the MiTF family of transcription factors is regulated downstream of mTORC1 in a uniquely FLCN and RagC^{GDP}-dependent manner (*7, 8*). Numerous studies corroborate the discovery of a "non-canonical" mTORC1 pathway that specifically regulates MiT-TFE transcription factors (*9, 18, 31-34*). The new knowledge of FLCN structural mechanism provided by the AFC structure can potentially be exploited for therapeutic benefit. The AFC presents itself as an attractive avenue for the long-standing goal of developing substrate selective mTORC1 inhibitors which can upregulate autophagy and lysosomal capacity without toxic consequences for immune function, epithelial renewal and other physiological processes that require mTORC1-dependent anabolic programs. Such inhibitors could be highly specific for MiT-TFE upregulation, in turn promoting autophagy and increasing lysosomal capacity. The latter could be of potential benefit for treating LSDs,

while both could potentially benefit neurodegenerative diseases involving intracellular protein aggregates. On the other hand, excessive upregulation of MiT-TFE transcription factors in FLCN loss of function has been shown to cause kidney cystogenesis, and tumorigenesis and induce melanoma (*7, 31*). Therapeutics that promote FLCN activity, for instance through inhibition of the LFC, might have potential for treating these conditions. An important consideration in therapeutic use of FLCN GAP antagonists would be to avoid the complete shutdown of FLCN activity and so avoid promoting tumorigenesis. The structural insights into the AFC presented here fulfill a key step necessary to leverage FLCN as a drug target and develop selective mTORC1 inhibitors or activators for MiT-TFE-dependent transcriptional upregulation.

Materials and Methods

Cloning and Protein Purification:

The pCAG-GST-SLC38A9^{NT}-FNIP2 fusion construct was designed to contain a ten-residue glycine-serine linker. Codon-optimized DNA coding for SLC38A9^{NT} and the C-terminal linker was amplified by polymerase chain reaction (PCR). DNA containing SLC38A9^{NT} and the C-terminal linker was subcloned into the pCAG-GST vector containing codon-optimized DNA coding for FNIP2. The pCAG-GST-FNIP2 vector was linearized using KpnI and XhoI restriction sites. DNA containing SLC38A9^{NT} and C-terminal linker was inserted N-terminal to FNIP2 by Gibson assembly. HEK293-GNTI cells were transfected with 1mg DNA at 2:1 ratio (FLCN: SLC38A9^{NT}-FNIP2) and 3mg P.E.I per 1L of cells at 2E6 cells/ml. Cells were pelleted at 2000 xg for 20 min at 4 °C and purified as described previously. *(8)*.

Mutants FLCN F10D and FNIP2 V146E were generated by site-directed mutagenesis using KAPA HiFi HotStart ReadyMix (Roche) from pCAG-FLCN and pCAG-GST-FNIP2 respectively. HEK293-GNTI cells were transfected with 1mg DNA at 2:1 ratio (FLCN:FNIP2) 3mg P.E.I per 1L of cells at 2E6 cells/ml. Cells were pelleted at 2000 xg for 20 min at 4 °C and purified as described previously *(8)*.

RagA:RagC^{D181N} and Ragulator were expressed and purified from Sf9 cells via baculovirus infection as described (*8*). GATOR1 was expressed and purified from HEK293-GNTI cells as described *(8)*.

Nucleotide Loading:

Purified RagA:RagC^{D181N} heterodimers were diluted 1:10 (v/v) in 1X phosphate-buffered saline (PBS) containing 5mM EDTA and 0.5 mM TCEP for 10 minutes at 25°C. Desired tri-phosphate nucleotides were added at a 10-fold molar excess over Rags and incubated for 30 minutes at 25°C. Next, $MgCl_2$ was added to a final concentration of 20 mM and incubated for 10 minutes at 25°C. Excess nucleotides were removed using a PD-10 desalting column (Cytiva) and wash buffer containing 25 mM HEPES, 130 mM NaCl, 2.5 mM $MgCl_2$, 2 mM EGTA, pH 7.4 and 0.5mM EDTA. To obtain the inactive state for Rag heterodimers, RagA^{GTP}:RagC^{XTP} was incubated with GATOR1 at a 1:100 GAP:Rag molar ratio at 37 °C for 30 minutes.

Active FLCN Complex Assembly:

To assemble the active FLCN complex, RagA:RagC^{D181N} heterodimers in desired nucleotide state were incubated for 1 hour at 25°C with a 1.2x molar excess of Ragulator. FLCN: SLC38A9^{NT}-FNIP2 was added to Rag-Ragulator complex at a 2-fold molar excess followed immediately by the addition of 0.5 M BeF_3. BeF_3 was prepared by mixing $BeSO_4$ and NaF to final concentration of 0.5mM and 5mM respectively and incubating for 20 minutes at 25°C prior to addition to complex. The complex containing Rags, Ragulator, FLCN: SLC38A9^{NT}-FNIP2 and BeF_3 was incubated at 25°C for 30 minutes, then at 4°C for 16 hours. Following incubation, the complex was centrifuged at 17,000 xg for 10 minutes and then loaded onto a Superose 6 (GE Healthcare) column equilibrated in wash buffer containing 25 mM HEPES, 130 mM NaCl, 2.5

mM $MgCl_2$, 2 mM EGTA, pH 7.4 and 0.5mM EDTA. Fractions were analyzed via SDS PAGE and those containing assembled active FLCN complex were collected, concentrated to 1 mg/ml and immediately frozen onto grids for imaging via cryo-EM.

Cryo-EM Grid Preparation and Imaging:

For data collection of active FLCN complex, 3 µl sample (1 mg/ml protein in 25 mM HEPES, 130 mM NaCl, 2.5 mM $MgCl_2$, 2 mM EGTA, 0.5 mM TCEP, pH 7.4) was deposited onto freshly glow-discharged (PELCO easiGlow, 45 s in air at 20 mA and 0.4 mbar) holey carbon grids (C-flat: 2/1-3Cu-T). FEI Virobot Mark IV was used to blot grids for 2 seconds with a blot force of 20 (Whatman 597 filter paper) at 4℃ and 90-100 % humidity and subsequentially plunged into liquid ethane. The Titan Krios G3i microscope equipped with a Gatan Quantum energy filter (slit width 20 eV) and a K3 summit camera at a defocus of -1.0 to -2.0 µm was used to record 4968 movies. Automated image acquisition was performed using SerialEM (*35*) recording four movies per 2 µm hole with image shift. Image parameters are summarized in Table S1.

Cryo-EM Data Processing:

The data processing workflow is summarized in Figure S1. In short, Relion-3.1.1 wrapped MotionCor2 program was used to motion-correct gain-corrected movies (*36, 37*). Motion-corrected micrographs were imported into cryosparc2 v3.3.1 (*38*). Patch CTF estimated (multi) was used for CTF determination and two rounds of cryosparc2 blob picker with a diameter range of 150Å-220Å was used to generate 1,165,732 and 1,025,735 particles. Particles were extracted with a box size of 440x440 pixels in cryosparc2. A series of 2D classifications followed by an ab-initio-reconstruction was used to generate three reference maps. The resulting 3D maps were used for consecutive rounds of heterogenous refinement from the initial particle sets following a round of 2D classification to remove obvious 'junk'. The resulting particle sets from round 1 and round 2 of picks were merged and duplicates were removed. The combined particle set contained 177,018 particles. A final round of homogenous refinement resulted in a 3.47Å map at 0.143 FSC. A mask was generated surrounding the interface between RagC and FLCN:FNIP2 using UCSF Chimera and imported into cryosparc2 v3.3.1 where it was lowpass filtered and dilated (*39*). The mask was used for subsequent local refinement and resulted in a focused map reaching a resolution of 3.16Å.

Atomic Model Building and Refinement:

The coordinates from RagC were based on GTP-bound crystal structure (3LLU), the coordinates for FLCN and FNIP2 were based off the LFC (6NZD) and all five Ragulator, RagA and $SLC38A9^{NT}$ were based on Rag-Ragulator-$SLC38A9^{NT}$ structure (6WJ2). All coordinates were rigid body fitted separately into the density map using UCSF Chimera. The interface was refined

using a map generated from local refinement separately by iterative rounds of Phenix real-space refinement and manual correction in coot (*40*). Secondary structure restrains were enabled during real-space refinement. The interface was combined with the remaining components of the complex in coot and refined using iterative round of Phenix real-space refinement and ISOLDE (*41*). The final model was validated using MolProbity (*42*). Coordinate models can be found in the Protein Data Bank (PDB) with accession code 8DHB.

Tryptophan Fluorescence RagC XTPase Assay:
Tryptophan fluorescence experiments were performed in triplicate according to *Fromm et al*. (*16*).

Cell Culturing:
HEK293T and HEK293A cells were grown in Dulbecco's modified Essential Media (DMEM, Thermo Fisher Scientific) supplemented with 10% (v/v) fetal bovine serum (FBS, VWR), 100 U/ml penicillin and 100 U/ml streptomycin (Life Technologies) and were maintained at 37 °C and 5% CO_2.

Reagents and Antibodies:
The following antibodies were employed in this study: phospho-T389 S6K1 (9234S), S6K1 (2708S), phospho-S65 4EBP (9451S), 4EBP (9644S and 9452S), FLCN (3697), TFE3 (14779), TFEB (37785), V5 (13202), FLAG (14793) from Cell Signaling Technology; LAMP2 (sc-18822) from Santa Cruz Biotechnology.

RNAi
The control pLKO.1-LUC shRNA vector and the pLKO.1-FLCN lentiviral shRNA vector were obtained respectively from Addgene (Plasmid #30324) and the RNAi Consortium (TRCN0000237886). Target sequences are:

shLUC: TCCTAAGGTTAAGTCGCCCTCG.
shFLCN: GATGGAGAAGCTCGCTGATTT

RNAi experiments were prepared as described below.

Lentiviral Infection and Stable Cell Line Generation:
Lentivirus was generated using the PEI method. 5 µg of a lentiviral vector (desired construct in pLJM1-PURO) was combined with 3.75 µg of psPAX2 and 1.25 µg pCMG.2 viral packaging plasmids in 500 µl optiMEM (Thermofisher), mixed, and then combined with 60 µl 1 mg/mL P.E.I. This solution was incubated at room temperature for 30 minutes, then added to a 10 cm dish containing 2 million recently plated 293T cells.
24-48 hours after that, media containing virus was collected from cells, spun down at 1,300 x rpm

for 5 minutes to remove cell debris, and sterile filtered. Cells were plated at a density of 200,000-300,000 cells per well in a 6-well plate in the presence of Polybrene transfection reagent (Sigma-Aldrich) and infected with 10% of the total virus from one 10 cm plate of the indicated constructs. 24 hours later, media was supplemented with 200 nM puromycin.

Live Cell Treatment:

HEK293T cells were seeded and allowed to attach overnight in complete DMEM medium. 24h after seeding, cells were rinsed with PBS and incubated in amino acid-free RPMI for 2 hours (-AA) and restimulated with amino acids for 15 minutes or overnight with complete media (+AA). Amino acid solutions were prepared from powders and the final concentration of amino acids in the media was the same as in commercial RPMI. Torin1 treatment was performed for 4 hours in complete media.

Western Blotting:

HEK-293T cells were plated in a 6-well plate at 1,000,000 cells/well in complete media. After the treatments (see above), the medium was removed and 150 µl of Lysis Buffer (40 mM HEPES [pH 7.4], 4 mM EDTA, 1% Triton X-100, 10 mM sodium β-glycerol phosphate, 10 mM sodium pyrophosphate, and one tablet of EDTA-free protease inhibitors per 50 ml) were added to each well. Total extracts were collected from each well after scraping, rotated over-end for 10 minutes, and then centrifuged at 13,000 × g for 10 min at 4 °C. Samples were normalized to a total concentration of 1 mg/mL protein and combined with protein sample buffer, then boiled for 5 minutes at 95 °C. Ten micrograms of protein were loaded into each lane of Tris-Glycine precast gels (Thermo Fisher Scientific). PVDF membranes were blocked in 5% skim milk dissolved in Tris-buffered saline with Tween 20 for 1 hour at RT. Membranes were incubated overnight at 4 °C with the indicated primary antibodies, all diluted in 5% skim milk prepared in TBST. Secondary antibodies conjugated to horseradish peroxidase were used for protein detection. β-Actin was used as loading controls.

Immunofluorescence:

HEK-293T cells were plated on fibronectin-coated glass coverslips in 12-well plates, at 300,000 cells/well. The following day, cells were subjected to amino acid depletion/or complete media restimulation (see above) and then fixed in 4% paraformaldehyde (in PBS) for 15 min at RT. The coverslips were rinsed twice with PBS and cells were permeabilized with 0.1% (w/v) saponin in PBS for 10 min. After rinsing twice with PBS, the slides were incubated overnight at 4°C with the indicated primary antibody in 5% normal donkey serum, then rinsed with PBS, and incubated with fluorophore-conjugated secondary antibodies produced in goat or donkey (Life Technologies, diluted 1:500 in 5% normal donkey serum) for 45 min at room temperature in the dark. Coverslips were then washed three times in PBS and mounted on glass slides using Vectashield Antifade

Mounting Medium (Vector Laboratories) containing DAPI stain. All images were collected on a Nikon Ti-E inverted microscope (Nikon Instruments, Melville, NY) equipped with a Plan Apo 60x oil objective. Images were acquired using a Zyla 5.5 sCMOS camera (Andor Technology), using iQ3 acquisition software (Andor Technology).

Live Imaging:

HEK293A cells were plated onto glass-bottom 35mm culture dishes and transfected with the Indicated FLCN-FLAG-eGFP, HA-FNIP2, and LAMP2-RFP-FLAG constructs. The following day, cells were subjected to amino acid depletion/or amino acids restimulation (see above). Starved cells were transferred to imaging buffer (10 mM HEPES, 136 mM NaCl, 2.5 mM KCl, 2 mM CaCl2, 1.2 mM MgCl2, pH 7.4), while restimulated cells were transferred to imaging buffer supplemented with amino acids, 5mM glucose, and 1% dialyzed FBS (+AA) and imaged using the Nikon Ti-E inverted microscope (Nikon Instruments, Melville, NY) as explained above.

Quantitation of Lysosomal Enrichment Score:

For immunofluorescence and live imaging datasets, a home-built MATLAB (Mathworks) script was used to determine the lysosomal enrichment of both V5-FNIP2 and FLAG-FLCN stains as previously described (*9*). Briefly, a single cell was manually selected in the lamp channel and its nucleus was excluded from further analysis. Then, a mask was created in the LAMP2 channel to segment cellular pixels into LAMP2 (lysosomal) or non-LAMP2 (cytosolic) pixels. This mask was then applied to the non-LAMP2 channel. The Lysosomal Enrichment Score was determined by dividing the average intensity of pixels in the lysosomal region by the average intensity of the pixels in the cytosolic region. For each condition, at least twenty cells were analyzed from different multi-channel images.

Quantitation of Cytoplasmic:Nuclear TFE3 Ratio:

To measure TFE3 nuclear localization, the Pearson's coefficient of at least 10 different fields was measured using the ImageJ plugin JACoP (*43*).

References

1. R. A. Saxton, D. M. Sabatini, mTOR Signaling in Growth, Metabolism, and Disease. *Cell* **168**, 960-976 (2017).

2. R. E. Lawrence, R. Zoncu, The lysosome as a cellular centre for signalling, metabolism and quality control. *Nat Cell Biol* **21**, 133-142 (2019).

3. S. S. Schalm, D. C. Fingar, D. M. Sabatini, J. Blenis, TOS motif-mediated raptor binding regulates 4E-BP1 multisite phosphorylation and function. *Curr Biol* **13**, 797-806 (2003).

4. H. Nojima *et al.*, The mammalian target of rapamycin (mTOR) partner, raptor, binds the mTOR substrates p70 S6 kinase and 4E-BP1 through their TOR signaling (TOS) motif. *J Biol Chem* **278**, 15461-15464 (2003).

5. M. Sardiello *et al.*, A gene network regulating lysosomal biogenesis and function. *Science* **325**, 473-477 (2009).

6. C. Settembre *et al.*, A lysosome-to-nucleus signalling mechanism senses and regulates the lysosome via mTOR and TFEB. *EMBO J* **31**, 1095-1108 (2012).

7. G. Napolitano *et al.*, A substrate-specific mTORC1 pathway underlies Birt-Hogg-Dubé syndrome. *Nature* **585**, 597-602 (2020).

8. R. E. Lawrence *et al.*, Structural mechanism of a Rag GTPase activation checkpoint by the lysosomal folliculin complex. *Science* **366**, 971-977 (2019).

9. S. Wada *et al.*, The tumor suppressor FLCN mediates an alternate mTOR pathway to regulate browning of adipose tissue. *Genes Dev* **30**, 2551-2564 (2016).

10. T. Sekiguchi, E. Hirose, N. Nakashima, M. Ii, T. Nishimoto, Novel G proteins, Rag C and Rag D, interact with GTP-binding proteins, Rag A and Rag B. *J Biol Chem* **276**, 7246-7257 (2001).

11. Y. Sancak *et al.*, Ragulator-Rag complex targets mTORC1 to the lysosomal surface and is necessary for its activation by amino acids. *Cell* **141**, 290-303 (2010).

12. K. Shen, A. Choe, D. M. Sabatini, Intersubunit Crosstalk in the Rag GTPase Heterodimer Enables mTORC1 to Respond Rapidly to Amino Acid Availability. *Mol Cell* **68**, 552-565 e558 (2017).

13. Z. Y. Tsun *et al.*, The folliculin tumor suppressor is a GAP for the RagC/D GTPases that signal amino acid levels to mTORC1. *Mol Cell* **52**, 495-505 (2013).

14. L. Bar-Peled *et al.*, A Tumor suppressor complex with GAP activity for the Rag GTPases that signal amino acid sufficiency to mTORC1. *Science* **340**, 1100-1106 (2013).

15. S. Wang *et al.*, Metabolism. Lysosomal amino acid transporter SLC38A9 signals arginine sufficiency to mTORC1. *Science* **347**, 188-194 (2015).

16. S. A. Fromm, R. E. Lawrence, J. H. Hurley, Structural mechanism for amino acid-dependent Rag GTPase nucleotide state switching by SLC38A9. *Nat Struct Mol Biol* **27**, 1017-1023 (2020).

17. M. Rebsamen *et al.*, SLC38A9 is a component of the lysosomal amino acid sensing machinery that controls mTORC1. *Nature* **519**, 477-481 (2015).

18. K. Li *et al.*, Folliculin promotes substrate-selective mTORC1 activity by activating RagC to recruit TFE3. *PLoS Biol* **20**, e3001594 (2022).

19. G. Napolitano, C. Di Malta, A. Ballabio, Non-canonical mTORC1 signaling at the lysosome. *Trends Cell Biol*, (2022).

20. K. Shen *et al.*, Cryo-EM Structure of the Human FLCN-FNIP2-Rag-Ragulator Complex. *Cell* **179**, 1319-1329 e1318 (2019).

21. A. J. Fisher *et al.*, X-ray structures of the myosin motor domain of Dictyostelium discoideum complexed with MgADP.BeFx and MgADP.AlF4. *Biochemistry* **34**, 8960-8972 (1995).

22. J. H. Jeong *et al.*, Crystal structure of the Gtr1p(GTP)-Gtr2p(GDP) protein complex reveals large structural rearrangements triggered by GTP-to-GDP conversion. *J Biol Chem* **287**, 29648-29653 (2012).

23. M. Anandapadamanaban *et al.*, Architecture of human Rag GTPase heterodimers and their complex with mTORC1. *Science* **366**, 203-210 (2019).

24. E. Mihai Gazdag *et al.*, Mechanism of Rab1b deactivation by the Legionella pneumophila GAP LepB. *EMBO Rep* **14**, 199-205 (2013).

25. K. Gavriljuk *et al.*, Catalytic mechanism of a mammalian Rab.RabGAP complex in atomic detail. *Proc Natl Acad Sci U S A* **109**, 21348-21353 (2012).

26. W. Tian, C. Chen, X. Lei, J. Zhao, J. Liang, CASTp 3.0: computed atlas of surface topography of proteins. *Nucleic Acids Res* **46**, W363-W367 (2018).

27. M. Y. Su, S. A. Fromm, J. Remis, D. B. Toso, J. H. Hurley, Structural basis for the ARF GAP activity and specificity of the C9orf72 complex. *Nat Commun* **12**, 3786 (2021).

28. M. Y. Su, S. A. Fromm, R. Zoncu, J. H. Hurley, Structure of the C9orf72 ARF GAP complex that is haploinsufficient in ALS and FTD. *Nature* **585**, 251-255 (2020).

29. K. Shen, M. L. Valenstein, X. Gu, D. M. Sabatini, Arg-78 of Nprl2 catalyzes GATOR1-stimulated GTP hydrolysis by the Rag GTPases. *J Biol Chem* **294**, 2970-2975 (2019).

30. S. B. Egri *et al.*, Cryo-EM structures of the human GATOR1-Rag-Ragulator complex reveal a spatial-constraint regulated GAP mechanism. *Mol Cell*, (2022).

31. N. Alesi *et al.*, TSC2 regulates lysosome biogenesis via a non-canonical RAGC and TFEB-dependent mechanism. *Nat Commun* **12**, 4245 (2021).

32. J. M. Goodwin *et al.*, GABARAP sequesters the FLCN-FNIP tumor suppressor complex to couple autophagy with lysosomal biogenesis. *Sci Adv* **7**, eabj2485 (2021).

33. B. S. Gosis *et al.*, Inhibition of nonalcoholic fatty liver disease in mice by selective inhibition of mTORC1. *Science* **376**, eabf8271 (2022).

34. M. Paquette *et al.*, Loss of hepatic Flcn protects against fibrosis and inflammation by activating autophagy pathways. *Sci Rep* **11**, 21268 (2021).

35. D. N. Mastronarde, Automated electron microscope tomography using robust prediction of specimen movements. *J Struct Biol* **152**, 36-51 (2005).

36. S. H. Scheres, RELION: implementation of a Bayesian approach to cryo-EM structure determination. *J Struct Biol* **180**, 519-530 (2012).

37. S. Q. Zheng *et al.*, MotionCor2: anisotropic correction of beam-induced motion for improved cryo-electron microscopy. *Nat Methods* **14**, 331-332 (2017).

38. A. Punjani, J. L. Rubinstein, D. J. Fleet, M. A. Brubaker, cryoSPARC: algorithms for rapid unsupervised cryo-EM structure determination. *Nat Methods* **14**, 290-296 (2017).

39. E. F. Pettersen *et al.*, UCSF Chimera--a visualization system for exploratory research and analysis. *J Comput Chem* **25**, 1605-1612 (2004).

40. P. Emsley, B. Lohkamp, W. G. Scott, K. Cowtan, Features and development of Coot. *Acta Crystallogr D Biol Crystallogr* **66**, 486-501 (2010).

41. T. I. Croll, ISOLDE: a physically realistic environment for model building into low-resolution electron-density maps. *Acta Crystallogr D Struct Biol* **74**, 519-530 (2018).

42. C. J. Williams *et al.*, MolProbity: More and better reference data for improved all-atom structure validation. *Protein Sci* **27**, 293-315 (2018).

43. S. Bolte, F. P. Cordelieres, A guided tour into subcellular colocalization analysis in light microscopy. *J Microsc* **224**, 213-232 (2006).

Acknowledgements: We thank Zhicheng Cui and Aaron Joiner for discussions, Andrea Ballabio for comments on the manuscript, Rick Hooy for workstation support and Dan Toso and Jonathan Remis for electron microscope support.

Funding: This work was supported by the NIH grants R01 GM111730 (J.H.H.) and R01 GM130995 (R.Z.), a National Science Foundation Graduate Research Fellowship (R.M.J.), and an Italian Cancer Research Association (AIRC) postdoctoral fellowship (R.P.).

Author contributions: R.M.J. and J.H.H. conceived and designed research, R.M.J. and R.P. carried out research, A.L.Y. and S.F. trained R.M.J. in cryo-EM, R.Z. and J.H.H. supervised research, R.M.J. and J.H.H. wrote the first draft, and all authors edited the manuscript.

Competing interests: J.H.H. is a co-founder and shareholder of Casma Therapeutics and receives research funding from Casma Therapeutics, Genentech, and Hoffmann-La Roche. R.Z. is a cofounder and shareholder of Frontier Medicines and receives research funding from Genentech.

Data and materials availability: All data needed to evaluate the conclusions in the paper are present in the paper and/or the Supplementary Materials. Coordinates and density are deposited in the RCSB (PDB ID 8DHB) and EMDB (EMD-27435), respectively. The fusion construct used to generate the AFC is being deposited in Addgene.org.

Figure Legends

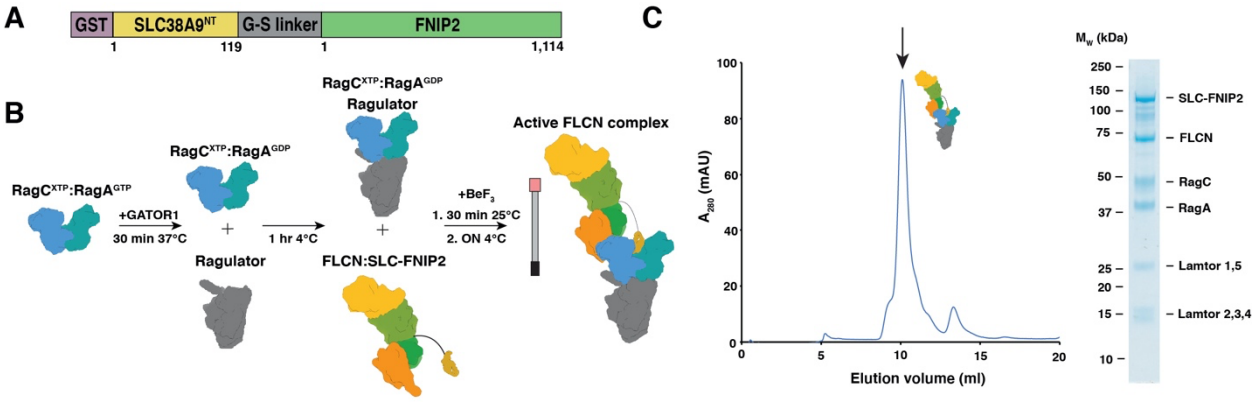

Figure 1. Active FLCN complex formation. (A) Construct design for SLC38A9^{NT}-FNIP2 fusion construct. (B) Complex formation workflow. (C) Size exclusion profile for active FLCN complex. Fraction containing all components of complex is labelled with a black arrow and visualized on adjacent gel.

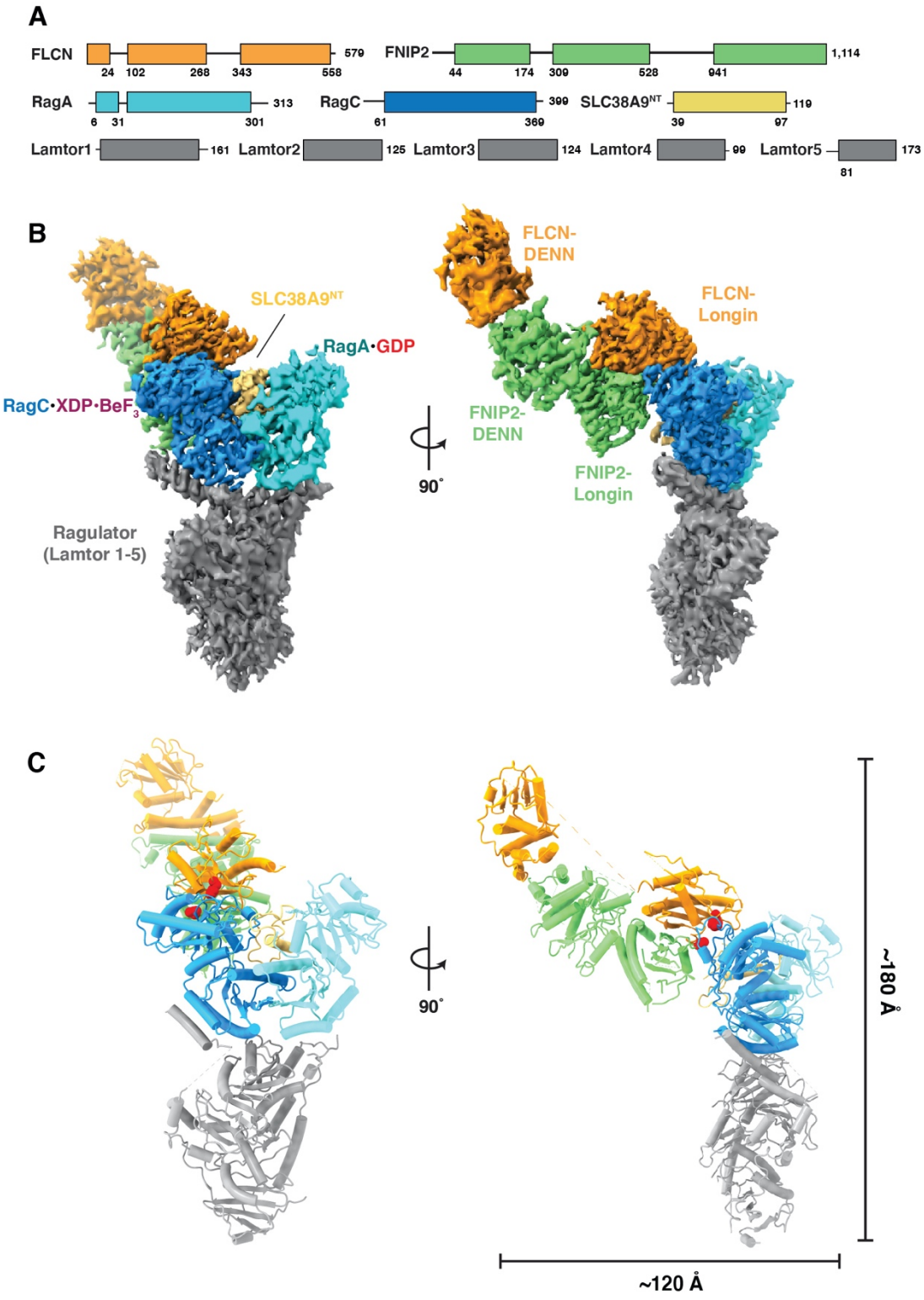

Figure 2. Cryo-EM structure of active FLCN complex. (A) Domain organization for components of active FLCN complex. (B) Composite map for complex. Focused map of interface was combined with overall map to produce composite map containing highest resolution information for each component. (C) Reconstructed model for AFC with overall

dimensions of the side view of the complex. Dotted regions in model represent unstructured regions in FLCN connecting the two domains. Red spheres indicated locations of mutations in FLCN F10D and FNIP2 V146E.

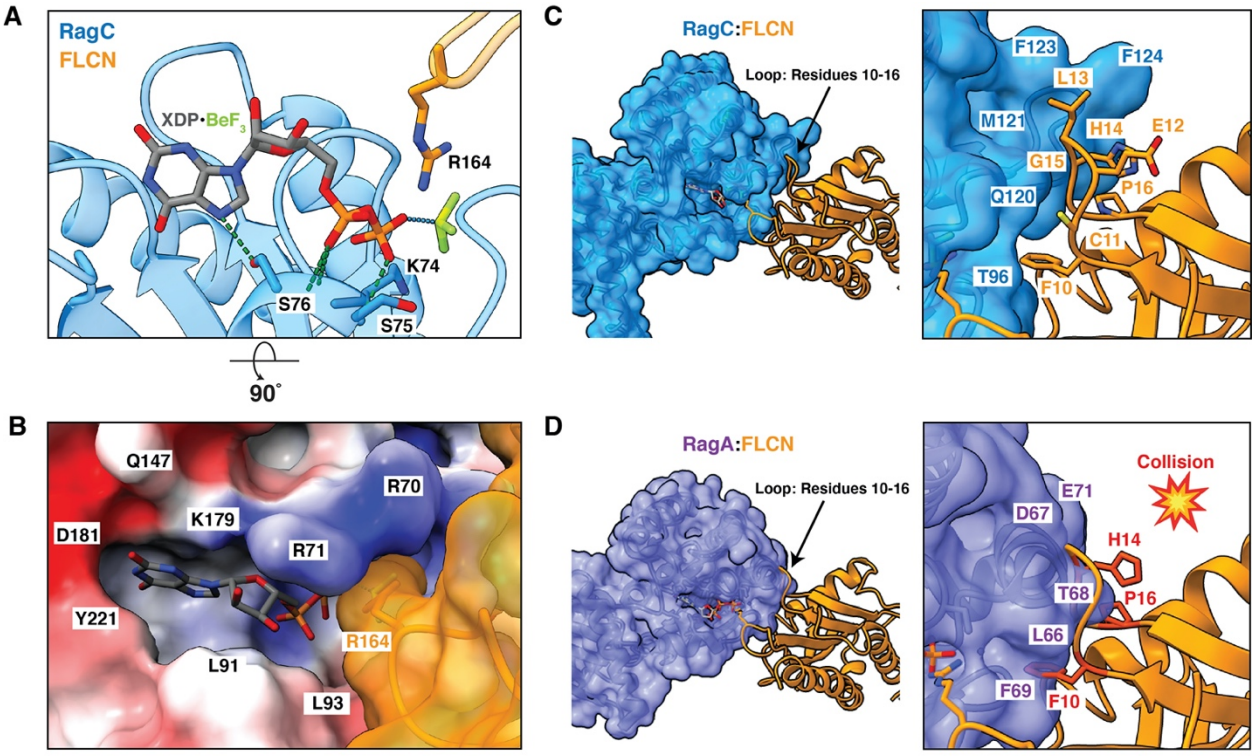

Figure 3. Specificity of FLCN-RagC GAP interaction in AFC. (A) Nucleotide binding pocket of RagC (blue) in AFC containing XDP-BeF_3 nucleotide analog. Location of FLCN (orange) arg-finger indicated. Hydrogen bonds between nucleotide and RagC residues (blue sticks) in surrounding pocket represented by dashed lines (green). (B) Surface representation of RagC binding site with FLCN arg-finger (orange). RagC colored based on electrostatic potential. (C) RagC (blue) FLCN (orange) interface in AFC. Loop residues 10-16 in FLCN indicated as sticks (black labels). (D) RagA (purple) FLCN interface modelled with GTP-bound RagA (PDB:6S6D). Residues in FLCN loop that clash with RagA are shown in red.

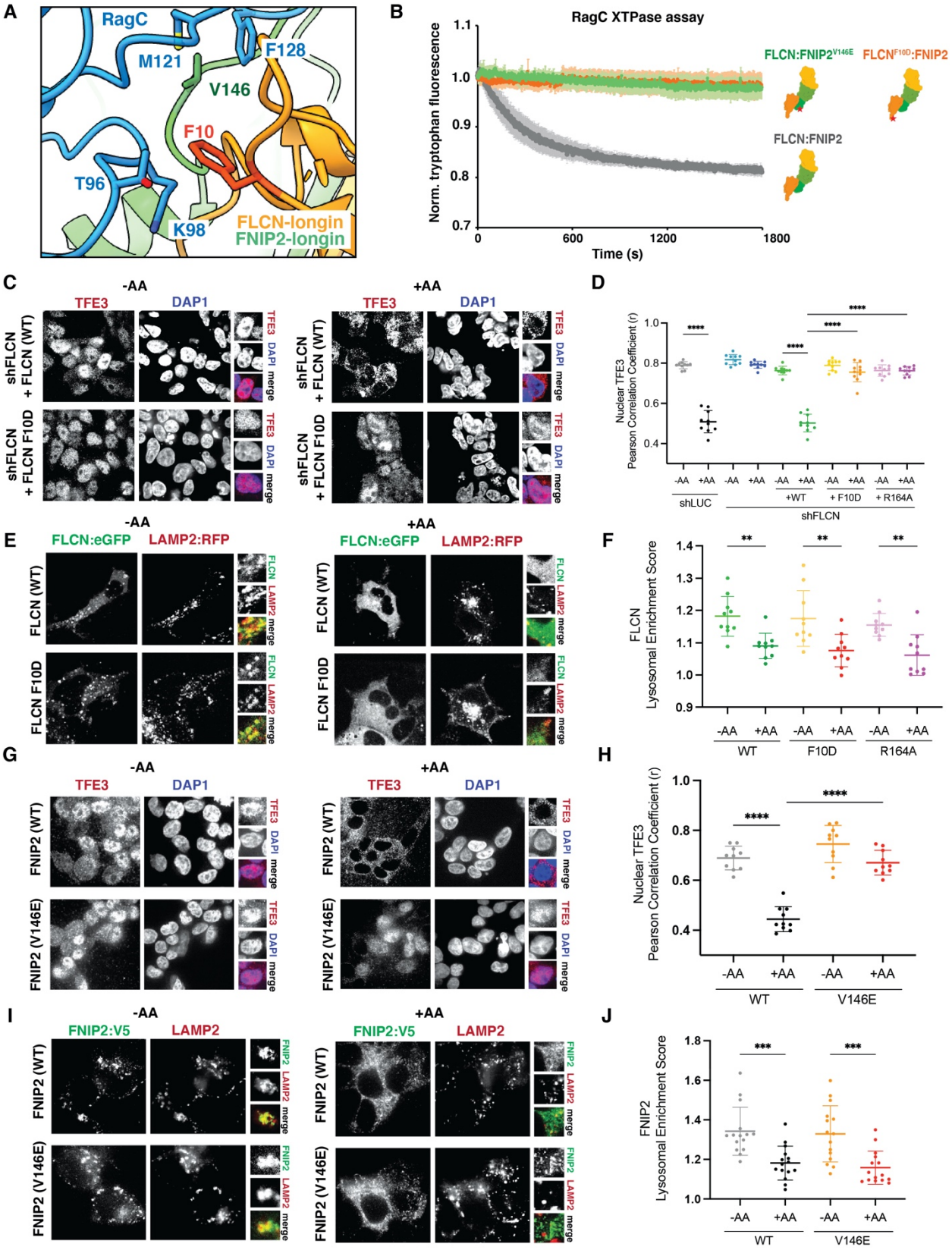

Figure 4. Hydrophobic residues in the FLCN:RagC interface necessary for GAP activity. (A) RagC (blue) and FLCN (orange):FNIP2 (green) interface in AFC. Position of FLCN:FNIP2 residues mutated at interface indicated. (B) Tryptophan fluorescence XTPase assay with FLCN: FNIP2 mutants. $FLCN^{WT}$: FNIP2 (gray), $FLCN^{F10D}$: FNIP2 (orange), or FLCN: $FNIP2^{V146E}$ (green) was incubated with $RagA^{GDP}$:$RagC^{XTP}$. Plotted are means ± SEM. n=3 replicates. (C) Immunofluorescence images of human embryonic kidney 293T (HEK293T) cells stably expressing the indicated genes shRNA targeting the indicated genes and FLCN rescue constructs. Cells were starved for 2 hours for amino acids (-AA) or restimulated with complete DMEM for 2 hours (+AA). (D) Quantification of TFE3 nuclear localization for immunofluorescence images and the positive control $FLCN^{164}$ identified previously (*8*) and shown in Fig. S8 immunofluorescence images (means ± SD, n = 10 fields for all conditions). **** $p< 0.0001$. (E) Fluorescence images of human embryonic kidney 293A (HEK293A) cells expressing the indicated FLCN:eGFP construct along with HA-FNIP2 and the lysosomal marker LAMP2:RFP. Cells were starved for 1 hour for amino acids (-AA) or starved and then restimulated with amino acids for 15 min (+AA). (F) Quantification of the lysosomal localization of over-expressed FLCN (lysosomal enrichment score) for immunofluorescence images (means ± SD, n = 15 cells for all conditions) ** $p< 0.01$. (G) Immunofluorescence images of HEK293T cells stably over-expressing the $FNIP2^{WT}$-eGFP-V5 or $FNIP2^{V146E}$-eGFP-V5 constructs. Cells were starved for 2 hours for amino acids (-AA) or maintained in complete media (+AA). (H) Quantification of TFE3 nuclear localization for immunofluorescence images (means ± SD, n=10 fields for all conditions) **** $p< 0.0001$. (I) Immunofluorescence images of human embryonic kidney 293T (HEK293T) cells stably over-expressing the indicated FNIP2-eGFP-V5 constructs. LAMP2 was used as lysosomal marker. Cells were starved for 2 hours for amino acids (-AA) or maintained in complete media (+AA). (J) Quantification of the lysosomal localization of over-expressed FNIP2 (lysosomal enrichment score) for immunofluorescence images (means ± SD, n = 15 cells for all conditions) *** $p< 0.001$.

Supplementary Materials

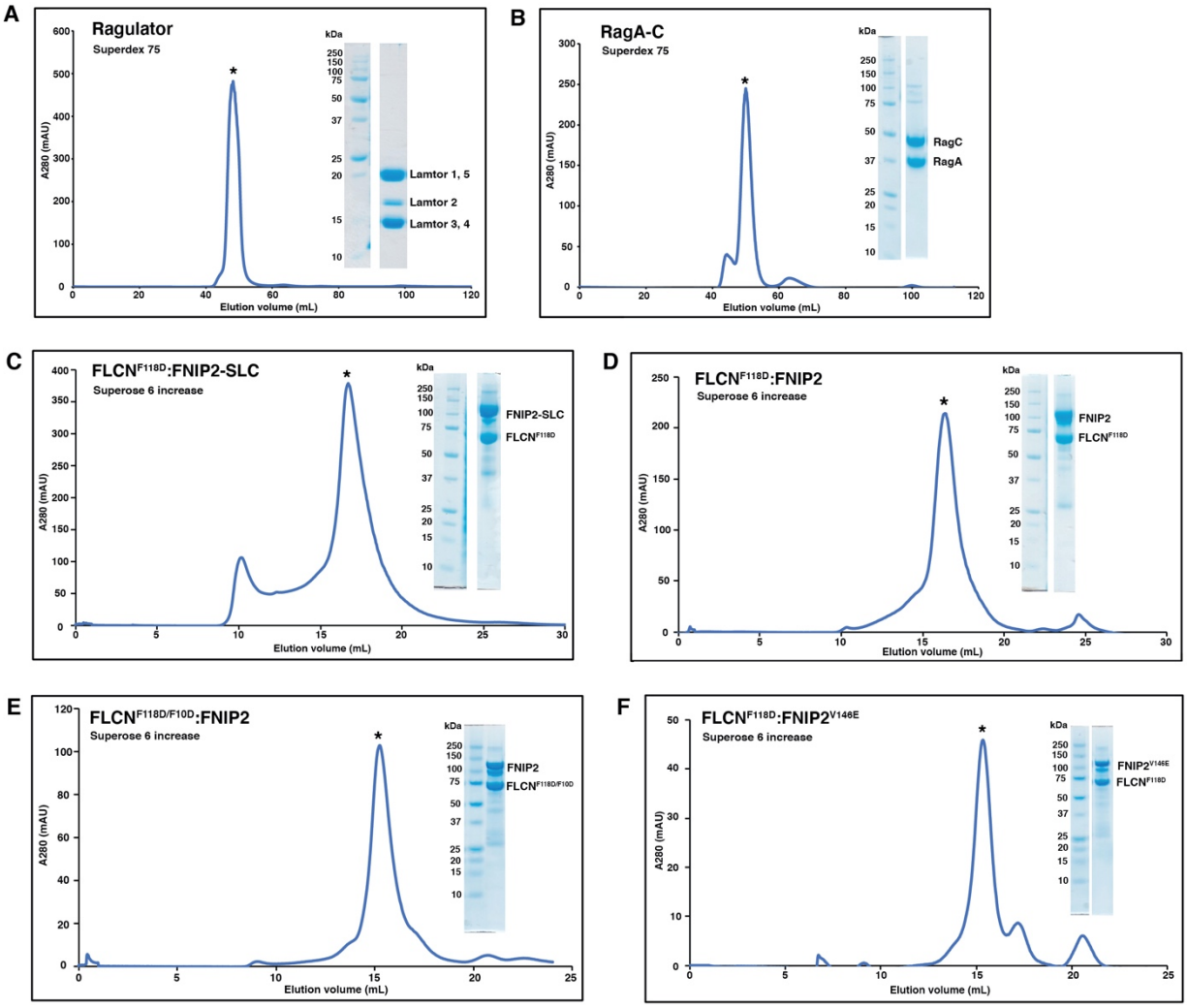

Fig. S1. Purification of individual active FLCN components. (A) Superdex 75 SEC elution profile for Ragulator and Coomassie blue stained SDS-PAGE analysis of protein sample collected from peak indicated with asterisk. (B) Superdex 75 SEC elution profile for Rag GTPases and Coomassie blue stained SDS-PAGE analysis of protein sample collected from peak indicated with asterisk. (C) Superose 6 increase SEC elution profile for FLCN^{F118D}:FNIP2-SLC fusion and Coomassie blue stained SDS-PAGE analysis of protein sample collected from peak indicated with asterisk. (D) Superose 6 increase SEC elution profile for FLCN^{F118D}:FNIP2 and Coomassie blue stained SDS-PAGE analysis of protein sample collected from peak indicated with asterisk. (E) Superose 6 increase SEC elution profile for FLCN$^{F118D/F10D}$:FNIP2 and Coomassie blue stained SDS-PAGE analysis of protein sample collected from peak indicated with asterisk. (F) Superose 6 increase SEC elution profile for FLCN^{F118D}:FNIP2^{V146E} and

Coomassie blue stained SDS-PAGE analysis of protein sample collected from peak indicated with asterisk.

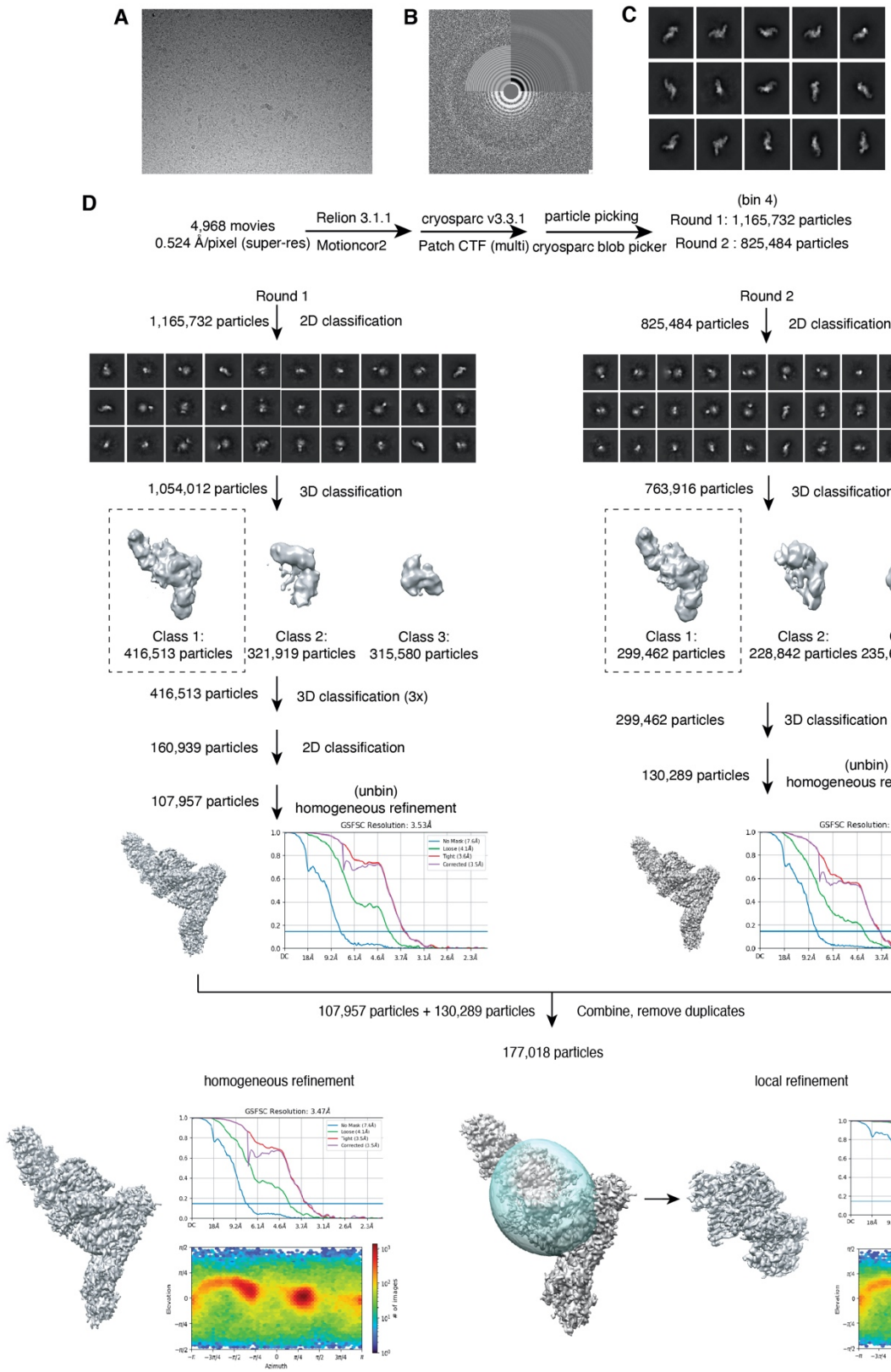

Fig. S2. Cryo-EM data processing pipeline. (A) Representative cryo-EM micrograph (B) Power spectrum and CTF estimation of micrograph shown in (A). Exemplary 2D class averages for the active FLCN complex. (D) Data processing pipeline for final map determination.

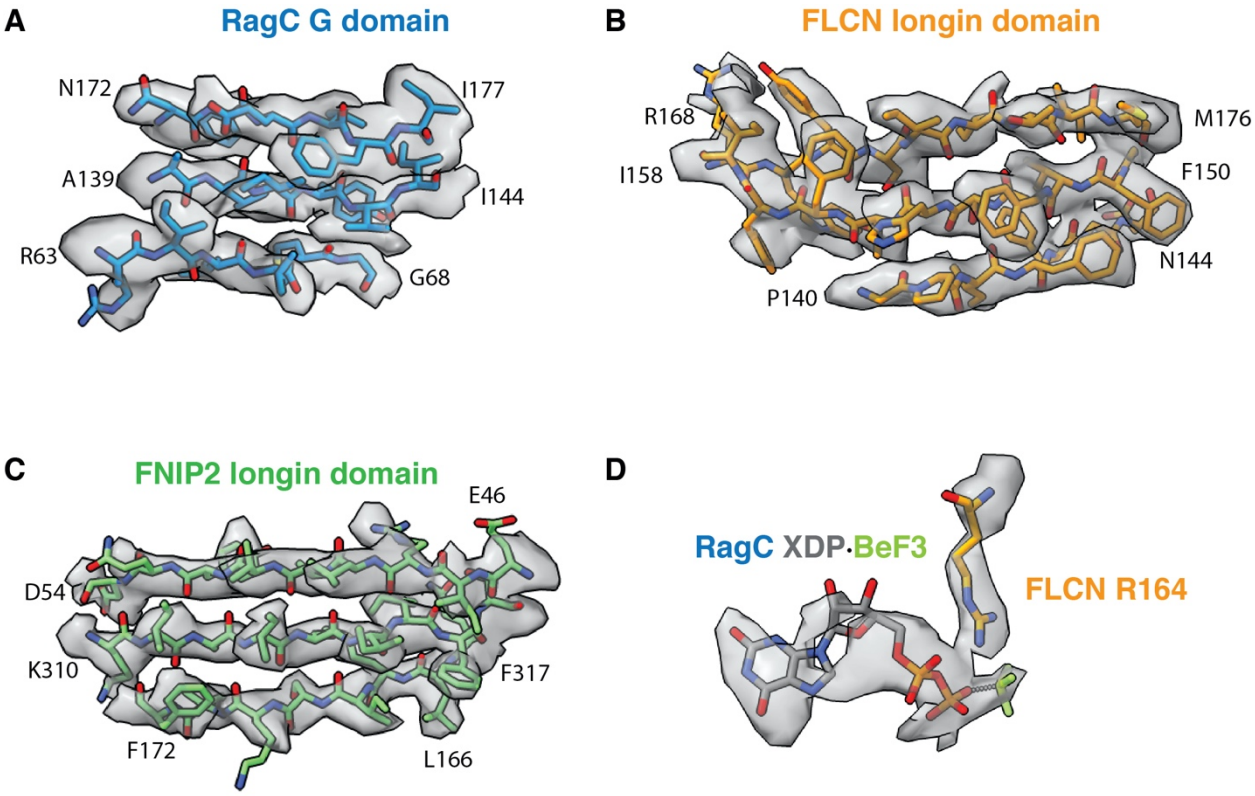

Fig. S3. AFC map-model fit. Representative refined coordinate model fit in cryo-EM density for (A) RagC (B) FLCN (C) FNIP2 (D) RagC nucleotide and FLCN arginine finger.

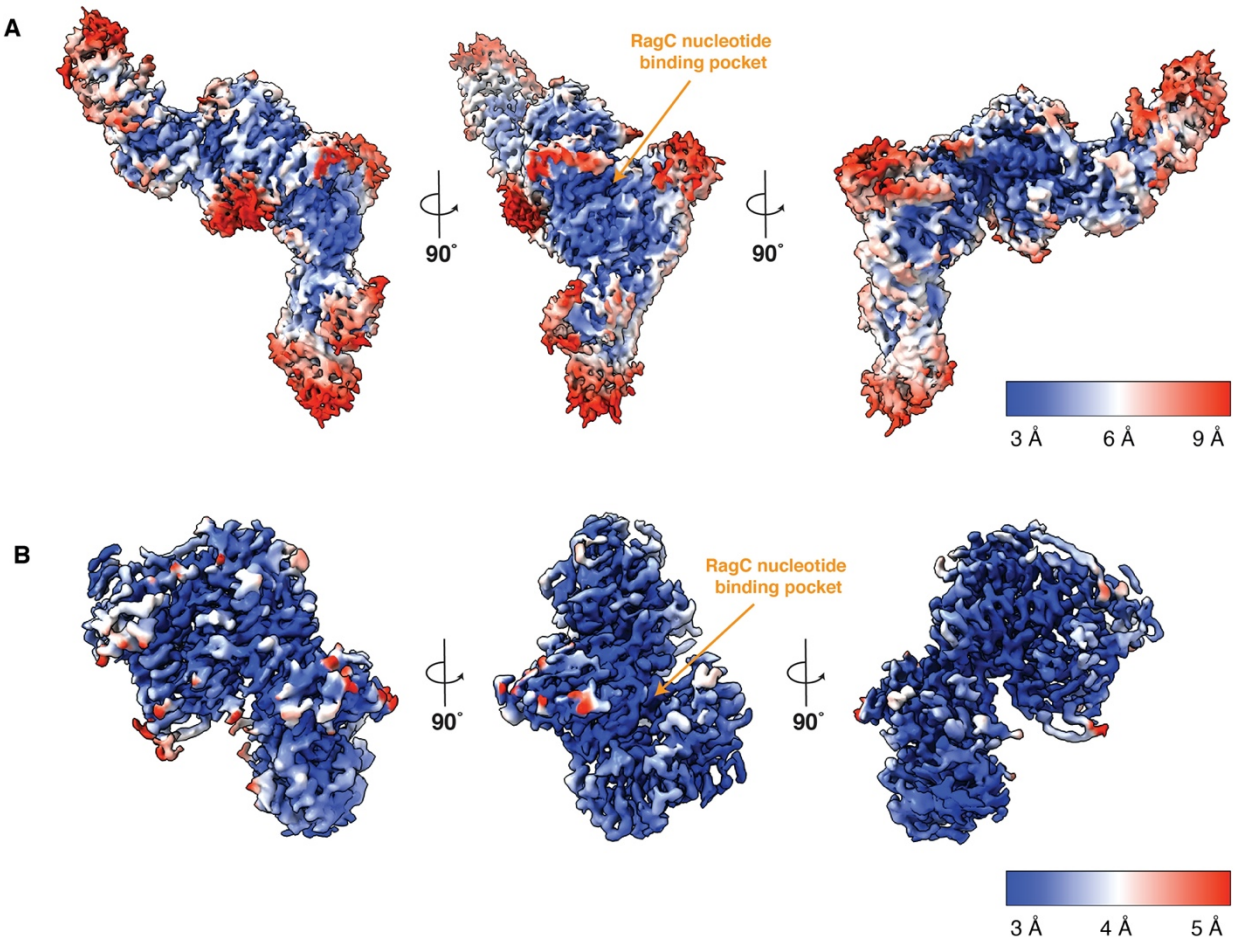

Fig. S4. AFC local resolution estimation. (A) Overall cryo-EM map for AFC colored according to local resolution. Resolution ranges from 3 Å to 9 Å. (B) Cryo-EM map of RagC – FLCN^{login}:FNIP2^{longin} interface generated from focused refinement colored according to local resolution. Resolution ranges from 3 Å to 6 Å.

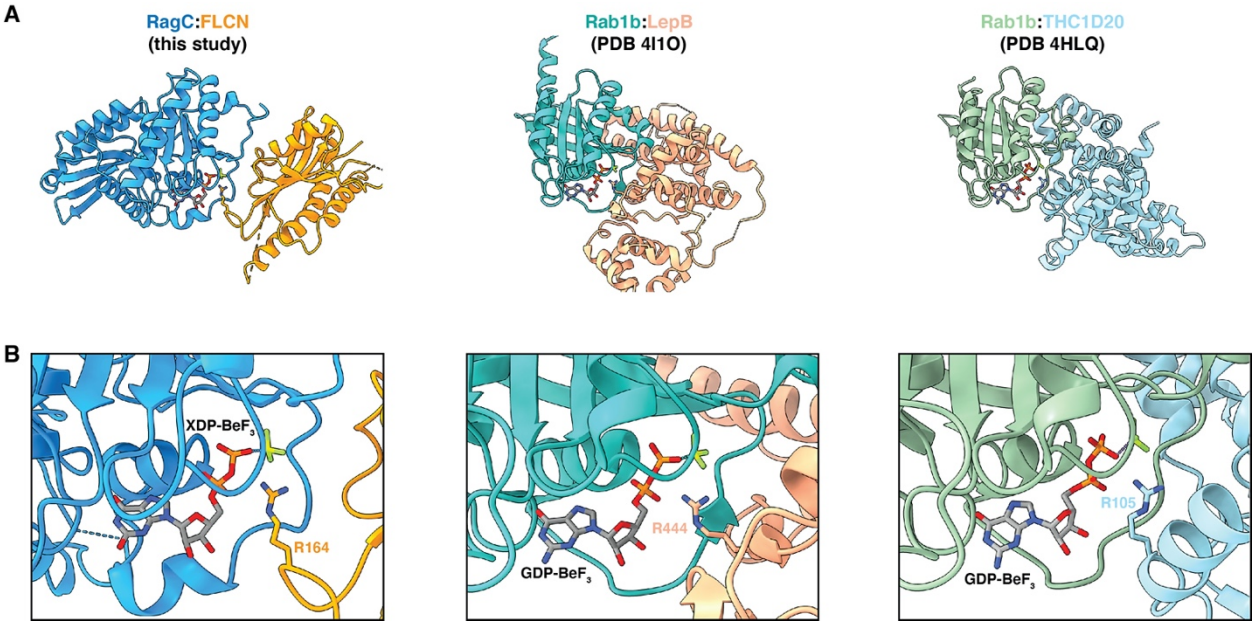

Fig. S5. Structural comparison between RagC:FLCN and other small GTPases:GAP. (A) Rab1b:LepB and Rab1b:THC1D20. (A) Structural comparison of RagC:FLCN (AFC structure), Rab1b:LepB (PDB 4I1O) and Rab1b:THC1D20 (PDB 4HLQ). Structures are shown in the same orientation. (B) Close-up of the nucleotide binding pocket with catalytic arginine-finger residue positioned in active site.

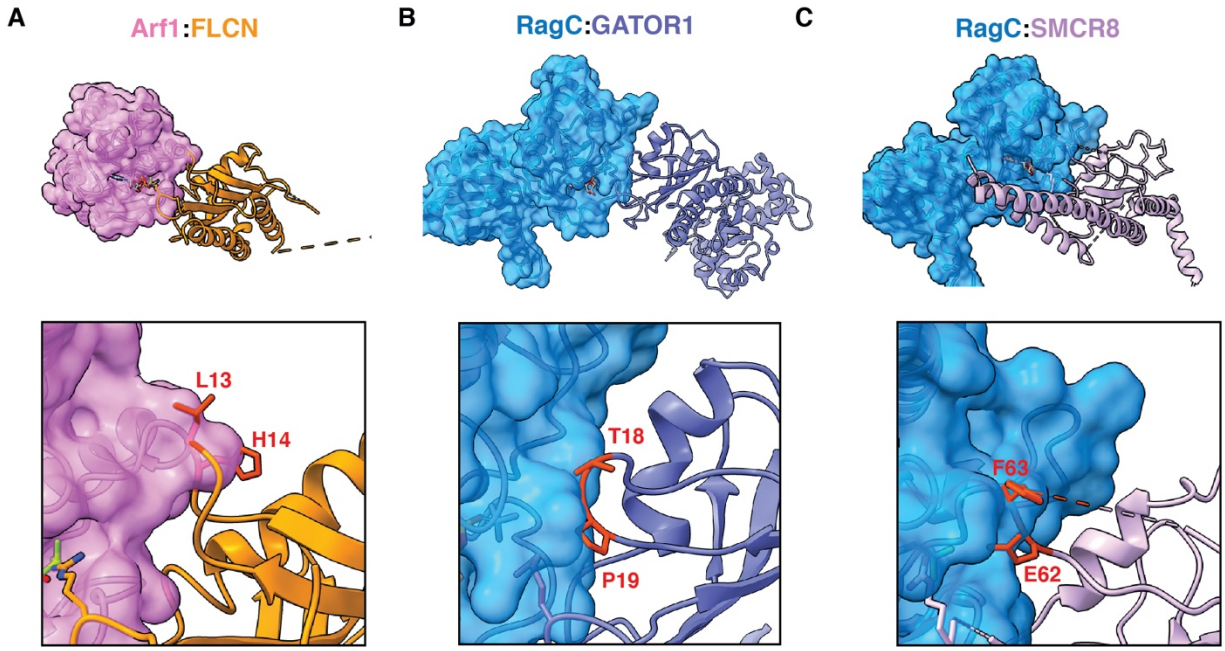

Fig. S6. Structural investigation of RagC:SMCR8 and Arf1:FLCN interface. (A) Model of Arf1 (pink) and FLCN (orange) interface generated by aligning Arf1 from Arf1:SMCR8 structure (PDB: 7MGE) with RagC in AFC structure (*27*). Residues in FLCN at interface that clash are indicated and labelled in red. (B) Model of RagC (pink) and SMCR8 (orange) interface generated by aligning SMCR8 from Arf1:SMCR8 structure (PDB: 7MGE) with FLCN in AFC structure (*27*). Residues in SMCR8 at interface that clash are indicated and labelled in red.

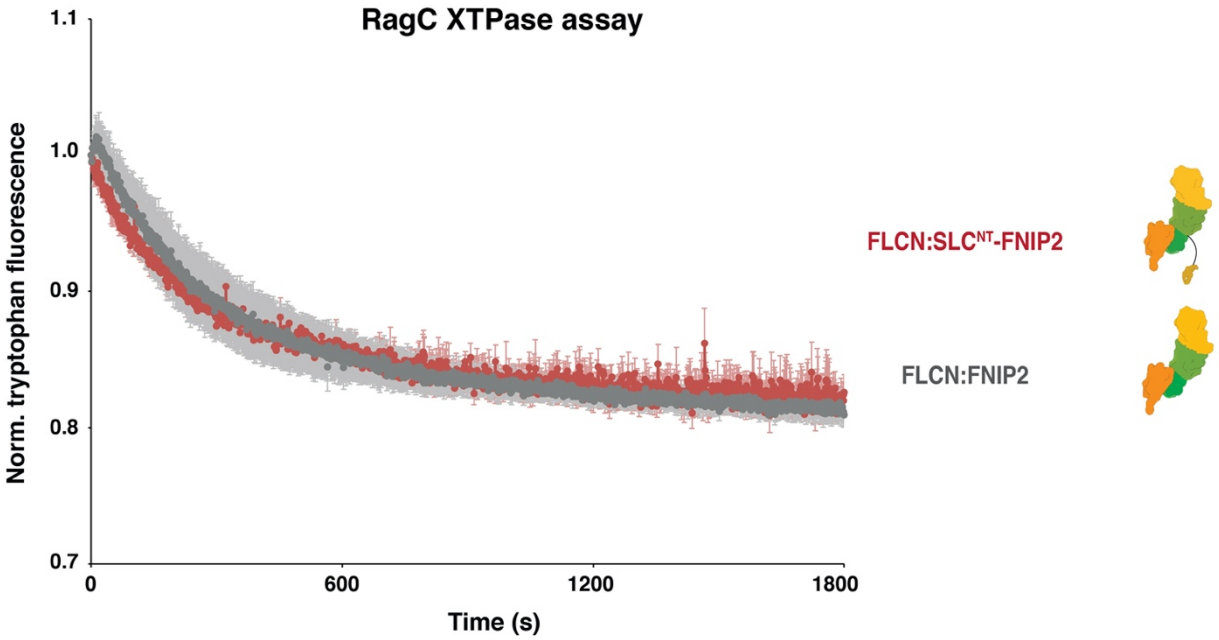

Fig. S7. GAP activity of FLCN:SLC-FNIP2. Tryptophan fluorescence XTPase assay with FLCN:SLC-FNIP2 fusion construct. $FLCN^{F118D}$: FNIP2 (gray), $FLCN^{F118D}$: SLC-FNIP2 (red), was incubated with $RagA^{GDP}$:$RagC^{XTP}$. Plotted are means ± SEM. n=3 replicates.

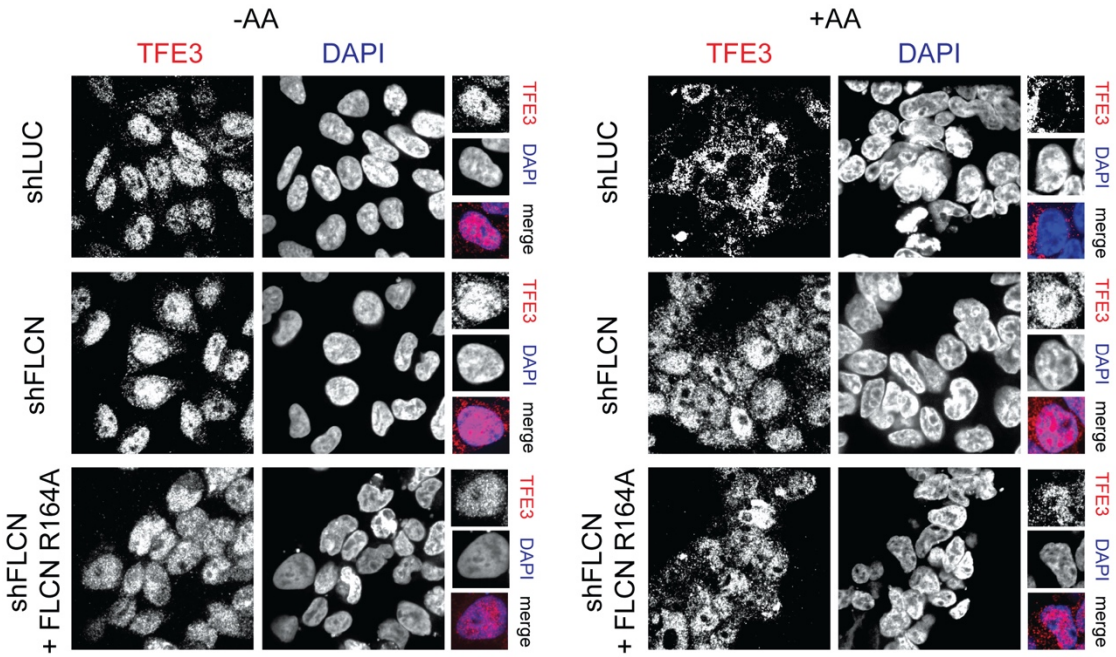

Fig. S8. Immunofluorescence for FLCN^{R164}. Immunofluorescence images of human embryonic kidney 293T (HEK293T) cells stably expressing the indicated genes shRNA and FLCN rescue constructs. Cells were starved for 2 hours for amino acids (-AA) or restimulated with complete DMEM for 2 hours (+AA).

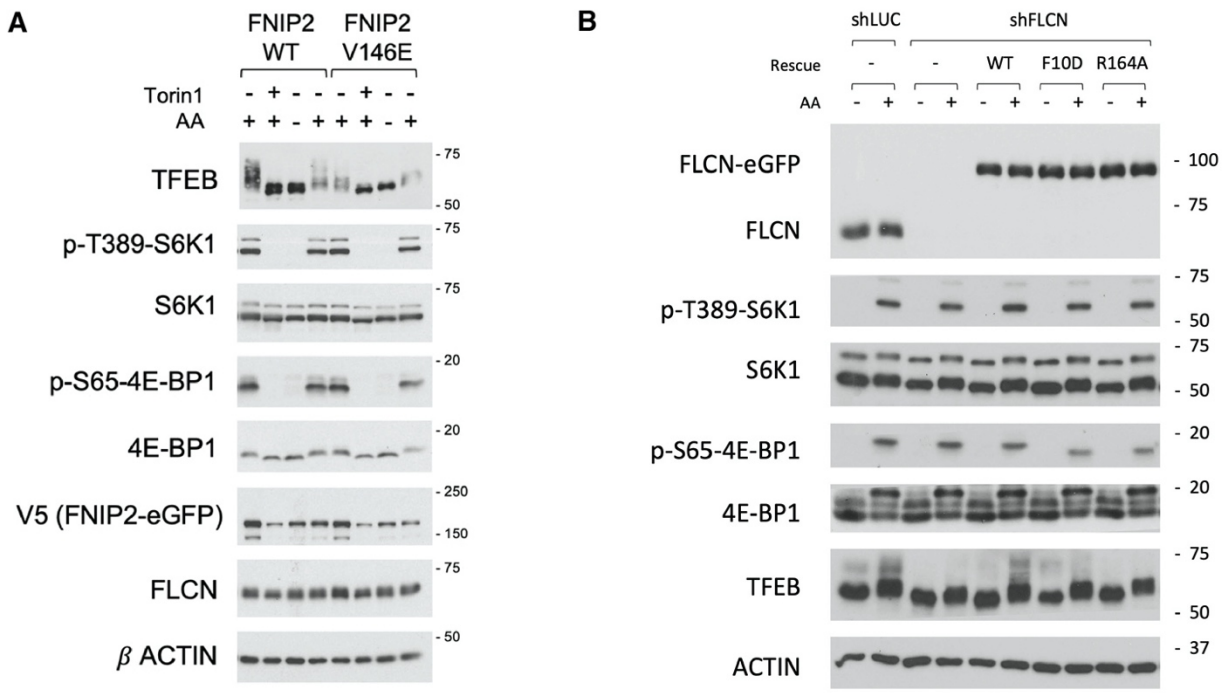

Fig. S9. Immunoblot analysis for mTORC1 targets. (A) HEK-293T cells stably expressing $FNIP2^{WT}$ or $FNIP2^{V146E}$ were either untreated or treated with Torin1, or starved for amino acids for 2 hours, or starved and then restimulated with amino acids for 15 minutes. Cells were lysed, followed by immunoblotting for the indicated proteins and phospho-proteins. (B) HEK-293T cells stably expressing shRNAs targeting the indicated genes were starved for amino acids for 2 hours, or starved and then restimulated with amino acids for 15 minutes. Cells were lysed, followed by immunoblotting for the indicated proteins and phospho-proteins.

Table S1.
Cryo-EM data acquisition and image processing.

	Active FLCN complex
Data acquisition	
Microscope	Titan Krios
Voltage (kV)	300
Camera	Quantum-K3 Summit
Magnification	165,000
Pixel size (Å)	0.524 (super-resolution)
Cumulative exposure ($e^-/Å^2$)	50
Energy filter slit width (eV)	20 eV
Defocus range (μm)	-1.0 to -2.0
Automation software	SerialEM
Exposure navigation	Image Shift
Number of movies	4968
Image processing	
Initial picked particles (no.)	Round 1: 1,165,732 Round 2: 825,484
Final refined particles (no.)	177,018
Map resolution (Å)	Overall: 3.53 Interface: 3.16
FSC threshold	0.143

Table S2.
AFC coordinate model refinement and assembly

PDB access code	8DHB
EMDB	EMD-27435
Refinement	
Software	Phenix 1.19, ISOLDE
Refinement target (Å)	3.2 (interface) 3.5 (overall)
Non-hydrogen atoms	15171
Residues	1898
Ligands	GDP (1) XDP-BeF^{-}_{3} (1)
RagA, Ragulator, $SLC38A9^{NT}$ reference PDB	6WJ2
FLCN:FNIP2 reference PDB	6NZD
RagC reference PDB	3LLU
Map-model statistics	
R.M.S deviations	
Bond lengths (Å)	0.006
Bonds angles (Å)	1.037
Validation	
Molprobitity	1.93
Clash score	8.98
Rotamer ouliers (%)	0
Cβ outliers (%)	0
CaBLAM outliers (%)	3.95
Ramachandran	
Favored (%)	92.97
Allowed (%)	6.7
Outlier (%)	0.33
Final model composition	
Number of chains	10
Number of Residues	1898
Ligands	2
B-factors	
Protein (min/max/average)	0.27/55.15/27.92
Ligands	10.59

Movie S1. Structural rearrangement of FLCN:FNIP2 between LFC and AFC. Visualization of the inactive (LFC) and active (AFC) binding modes of FLCN:FNIP2 to Rag-Ragulator. Red spheres indicated locations of mutations FLCN F10D and FNIP2 V146E.